Dalton Transactions

ROYAL SOCIETY OF CHEMISTRY

PAPER

View Article Online
View Journal | View Issue

Cite this: *Dalton Trans.*, 2025, **54**, 9208

Enhancing redox functionality in dinuclear europium complexes†

Nithin Suryadevara, ‡ Stanley Bagio, ‡ Moya A. Hay, Robert W. Gable and Colette Boskovic *

Europium stands out amongst the lanthanoid elements because of its accessibility in the divalent state, in addition to the more common trivalent state. To explore europium-based redox chemistry in the presence of redox-active ligands, we have synthesised a series of dinuclear europium complexes with different redox-active bridging ligands containing oxygen and nitrogen donor atoms. Here, we report three new dinuclear europium complexes containing different redox-active bridging ligands: $[\{Eu^{II}(I)_2(tpa)\}_2(\mu\text{-bpym})]$ (**1**), $[\{Eu^{III}(I)_2(tpa)\}_2(\mu\text{-bptz}^{\bullet-})][I]$ (**2**), and $[\{Eu^{III}(tpa)_2\}(\mu\text{-}Br_4cat)_3]$ (**3**) (tpa = tris(2-pyridylmethyl)amine; bpym = 2,2′-bipyrimidine; bptz = 3,6-bis(2-pyridyl)-1,2,4,5-tetrazine and Br_4catH_2 = tetrabromocatechol). Across the series, the varying oxidation states of europium and the bridging ligands highlight the redox diversity accessible with these compounds. Characterization using X-ray crystallography, electronic spectroscopy, electrochemistry, and magnetometry has allowed confirmation of the oxidation states of both the metal centers and the ligands, showcasing the rich redox chemistry of these molecular europium systems.

Received 6th February 2025,
Accepted 30th April 2025

DOI: 10.1039/d5dt00302d

rsc.li/dalton

Introduction

Although lanthanoid ions are predominantly studied in the trivalent state in which they are most stable, the divalent and tetravalent states are of increasing interest as routes to access new physical and chemical properties. Among the lanthanoid metals, europium stands out as the most readily accessible in both divalent and trivalent states, with distinct differences in the electronic structures enabling unique magnetic, redox and photophysical characteristics.[1–6] Europium compounds are presently employed in catalysis, optics and magnetic resonance imaging, and separation and recycling.[7–11] Advancing the understanding of their redox chemistry has the potential to enhance the application of europium compounds in diverse scientific and technological domains.[4,8,12,13]

Incorporating redox-active ligands into molecular lanthanoid chemistry can modulate the, magnetic and photophysical properties and reactivity.[7,14–17] For example, redox-active bridging ligands available in a radical oxidation state can provide additional magnetic interactions in dinuclear lanthanoid complexes, leading to enhanced single-molecule magnet behavior.[18–29] Furthermore, radical ligands can also impart distinct spectroscopic features, such as new electronic transitions and differences in luminescence properties.[16] Finally, redox-active ligands influence the redox potential of coordinated lanthanoid ions, thereby offering precise control over the electronic structure and resulting physical and chemical properties of lanthanoid compounds.[30–32] Despite the demonstrated impact of redox-active ligands in transition metal chemistry, their incorporation into europium systems remains comparatively underexplored.[4,8,33]

The redox capabilities of molecular europium compounds are extended in this work by introducing the redox-active ligands 2,2′-bipyrimidine (bpym), 3,6-bis(2-pyridyl)-1,2,4,5-tetrazine (bptz), and tetrabromocatechol (Br_4catH_2). Each of these ligands is potentially accessible in closed shell neutral and dianionic redox states, as well as a radical monoanionic form. Herein, we employ bpym, $bptz^{\bullet-}$ and Br_4cat^{2-} as bridging ligands in dinuclear Eu complexes that all feature tetradentate tris(2-pyridylmethyl)amine (tpa) blocking ligands. The tpa family of ligands has been used extensively in d-block chemistry,[34–38] but relatively little in f-element chemistry.[6,39] We report the synthesis and physical investigation of $[\{Eu^{II}(I)_2(tpa)\}_2(\mu\text{-bpym})]$ (**1**), $[\{Eu^{III}(I)_2(tpa)\}_2(\mu\text{-bptz}^{\bullet-})][I]$ (**2**), and $[\{Eu^{III}(tpa)_2\}(\mu\text{-}Br_4cat)_3]$ (**3**).

School of Chemistry, University of Melbourne, Parkville, Victoria 3010, Australia. E-mail: c.boskovic@unimelb.edu.au

†Electronic supplementary information (ESI) available: Additional thermogravimetric, powder X-ray diffraction, crystallographic and structural data, structural analysis, magnetic measurements, and UV-vis-NIR/diffuse reflectance. CCDC 2420256–2420258. For ESI and crystallographic data in CIF or other electronic format see DOI: https://doi.org/10.1039/d5dt00302d

‡Equal first authorship.

Experimental

Synthesis

Synthetic manipulation for **1** and **2** was performed under anaerobic conditions (N_2 atmosphere) using glovebox techniques unless otherwise mentioned. Compound **3** was synthesized under ambient conditions. Europium diiodide (EuI_2, yellow powder, >99.9% rare metal basis) was purchased from Sigma-Aldrich and used as received in the glovebox. Tris(2-pyridylmethyl)amine (tpa) was purchased from Combi-Blocks and was used after recrystallization from hexanes. $Eu(NO_3)_3{\cdot}6H_2O$ was purchased from Sigma-Aldrich and was used without any further purification. Diisopropyl ether (iPr_2O) was dried over molecular sieves (3 Å) for a minimum of 3 days and stored under N_2 on molecular sieves until used. Solvents – acetonitrile (MeCN) and tetrahydrofuran (THF) – were purified and dried using a solvent purification system (SPS) from MBraun (MB SPS-800, with standard MBraun drying columns). The solvents were degassed *via* three freeze–pump–thaw cycles before transferring them into the glovebox and were stored on molecular sieves inside the glovebox. The redox-active ligands – bpym, bptz and Br_4catH_2 – were prepared according to literature procedures.[40–42]

[{$Eu^{II}(I)_2(tpa)$}$_2$(μ-bpym)] (1). In a 14 mL screw-cap vial, EuI_2 (40.6 mg, 0.100 mmol) and tpa (29.1 mg, 0.100 mmol) were dissolved in MeCN (5 mL) to produce a bright orange solution. Separately, bpym (7.9 mg, 0.050 mmol) was dissolved in MeCN (2 mL) in another vial and the resulting solution was slowly added to the orange-coloured solution, which immediately became dark red (Fig. S1†). The mixture was stirred for 5 min and then allowed to settle for 10 minutes before filtering to remove the undissolved starting materials. THF was carefully layered on top of the dark red-coloured filtrate and then sealed with tape to prevent the loss of solvent. Dark red crystals suitable for single crystal X-ray diffraction were formed in a week and were collected by washing with THF, with crystallographic analysis suggesting the formulation **1**·2.5MeCN. The crystals collected were dried under several purge cycles in a glove box. Yield: 28 mg (35%). The bulk sample indicated partial desolvation, analyzing as **1**·MeCN; found: C 35.18, H 2.93, N 11.02; calc: C 34.72, H 2.85, N 11.44.

[{$Eu^{III}(I)_2(tpa)$}$_2$(μ-$bptz^{\bullet-}$)][I] (2). In a 14 mL screw-cap vial, EuI_2 (40.6 mg, 0.100 mmol) and tpa (29.1 mg, 0.100 mmol) were dissolved in MeCN (5 mL), to produce a bright orange solution. The bptz ligand (17.7 mg, 75.0 μmol) was suspended in iPr_2O (5 mL) in a different vial and was carefully layered on top of the above solution and then sealed with tape to prevent the loss of solvent. An immediate colour change from bright orange to purple-red was observed at the interface. Dark red crystals suitable for single crystal X-ray diffraction formed after a week, with crystallographic analysis indicating hydration [{$Eu^{III}(I)_2(tpa)$}$_2$(μ-$bptz^{\bullet-}$)][I]·$0.7H_2O$ (**2**·$0.7H_2O$). Crystals were collected by washing with iPr_2O and dried under several purge cycles in a glove box. Yield: 5 mg (6%). It was not possible to obtain an analytically pure bulk sample of this compound.

[{$Eu^{III}(tpa)_2$}(μ-$Br_4cat)_3$] (3). Complex **3** was synthesized under ambient conditions. In a 28 mL push-cap vial, $Eu(NO_3)_3{\cdot}6H_2O$ (51.4 mg, 0.120 mmol) was dissolved in dry MeCN (5 mL). In another vial, tpa (34.8 mg, 0.120 mmol) and Br_4catH_2 (76.6 mg, 0.180 mmol) were dissolved in dry MeCN (10 mL) and deprotonated with triethylamine (NEt_3) (50.1 μL, 36.4 mg, 0.360 mmol). The Br_4cat^{2-} and tpa mixture was then added dropwise to the $Eu(NO_3)_3$ solution, resulting in a yellow–orange solution (Fig. S3†). The solution was then gently agitated and left under ambient conditions for 48 hours, after which dark red crystals formed, with crystallographic analysis suggesting the formulation **3**·MeCN. The crystals were collected by vacuum filtration in air, washed with minimal MeCN and diethyl ether (Et_2O), and air dried. Yield: 54%. The bulk sample also analyzed as **3**·MeCN: found: C 30.67, H 1.87, N 5.45; calc: C 30.62, H 1.79, N 5.74.

Crystallography

Single-crystal X-ray diffraction data for complex **1** were collected at 100 K using a Rigaku Synergy X-ray diffractometer system using CuKα (λ = 1.5418 Å). The crystals of **1** were transferred into a closed vial with crystallographic oil inside a glovebox and quickly mounted onto the diffractometer under a cold N_2 gas stream to avoid contact with the atmosphere. The data were processed using CrysAlisPro software,[43] employing a numerical absorption correction based on Gaussian integration over a multifaceted crystal. Single-crystal X-ray diffraction data for compounds **2** and **3** were collected at 150 K and 100 K, respectively, on the MX2 beamline at the Australian Synchrotron,[44] tuned to approximately MoKα radiation (λ = 0.71076 Å) fitted with a silicon double crystal monochromator. Due to the sensitivity of the crystals of **2** to atmospheric oxidation, the crystals were carefully transferred in a closed vial under N_2 and the crystal for data collection was selected using a cold mount apparatus to avoid contact with the atmosphere. Data reduction was performed using XDS,[45] using strong multi-scan absorption correction in SADABS.[46] The structures of **2** and **3** were solved using CX-ASAP[47] and SHELXT,[48] while the structure of **1** was solved using SHELXT.[48] All three structures were refined using a full matrix least squares procedure based on F^2 using SHELXL[49] within OLEX2-1.5.[48,50,51] During structure refinement, all non-hydrogen atoms were refined with anisotropic displacement parameters while all hydrogen atoms were placed at geometric estimates and refined using the riding model with an isotropic displacement parameter of 1.2 U_{eq}. of the parent atom for all other atoms. The structure of **1** showed the presence of solvent voids filled with diffuse solvent. The contribution of the solvent to the diffraction pattern was modelled using the OLEX2 Solvent Mask routine; the electron density peaks were consistent with the presence of 1.5 molecules per formula unit. The structure of **2** showed electron density peaks close to the Eu and I atoms, suggesting some disorder of the complex. The I^- anion was modelled as being disordered over two positions with final occupancy factors of 0.921(3):0.079(3). Attempts to model the disorder of

the cation were unsuccessful, and so the refinement was continued without any modelling of the disorder.

Powder X-ray diffraction (PXRD) data were measured on a Rigaku Synergy dual wavelength rotating anode X-ray diffractometer system using CuK_α (λ = 1.5418 Å) at room temperature. Data were collected in the range $5 < 2\theta < 60°$ with an exposure time of 60 seconds per frame and processed using CrysAlisPro software.[43] The collected data were compared with powder patterns simulated from the crystal structures in Mercury.

Elemental analysis

The samples were sealed under vacuum into ampoules and analysed at the London Metropolitan University, London, United Kingdom.

Thermogravimetric analysis

Thermogravimetric analyses (TGA) were performed on a Mettler Moledo TGA/SDTA851e using a ramp rate of 5 °C min^{-1} to a maximum temperature of 400 °C under a flow of N_2.

Electronic spectroscopy

Diffuse reflectance ultraviolet-visible (UV-vis) spectra were collected for the samples diluted ~5% in KBr (inside a glove box for **1** and under ambient conditions for **3**) on a Thermo Scientific Evolution 220 UV-visible spectrophotometer. The diluted sample was placed into the quartz holder and the spectra were collected from 200 nm to 800 nm with a bandwidth of 3 nm. Solution measurements for **3** were performed using an Agilent Technology Cary 60 UV-visible spectrometer in CH_2Cl_2.

Magnetic measurements

The sample of **1** for magnetic measurements was prepared in a glovebox. The sample was weighed into an NMR tube with small amounts of eicosane inside the glovebox. A Young's valve was connected to the NMR tube and transferred to the Schlenk line. The sample tube was then flame sealed under vacuum. The sample of **3** was prepared under atmospheric conditions in gelatine capsules and sealed in eicosane.

The susceptibility and magnetization measurements were performed using a Quantum Design MPMS3 SQUID magnetometer. Susceptibility measurements were measured between 1.8 K and 300 K in an applied field H_{DC} = 1000 Oe (0.1 T). Magnetization (M) *vs.* field (H) measurements were performed between 0 and 7 T, at 2 K, 4 K and 6 K. The data were corrected for the diamagnetic contributions of the NMR tube and eicosane for **1**, while the diamagnetic contributions for the gelatine capsule and eicosane for **3** were also accounted for. The diamagnetic corrections for the molar magnetic susceptibilities were applied using Pascal's constants, approximated as MW/2 ($\times 10^{-6}$) emu mol^{-1}.[52] Fitting of magnetic susceptibility experimental data for **1** was performed using the PHI program, v3.1.5.[53]

Electrochemistry

All electrochemical measurements were performed under an N_2 atmosphere at room temperature and referenced to the ferrocene/ferrocenium (Fc/Fc^+) couple. The insolubility of **1**·MeCN in all standard solvents prevented conventional solution-state measurements, and therefore solid-state electrochemistry was performed instead. Voltammetric measurements were not performed on **2**·0.7H_2O due to the low yield and considerable air sensitivity. Voltammetric measurements of **3**·MeCN were performed in CH_2Cl_2.

In all cases, electrochemical measurements employed a three-electrode system, with a glassy carbon working electrode (1.0 mm for cyclic voltammetry and differential pulse voltammetry, 3.0 mm for rotating disc electrode voltammetry), a Pt/Ti auxiliary electrode, and an Ag/AgCl reference electrode. Cyclic voltammetry (CV) measurements were conducted at 100 mV s^{-1}, differential pulse voltammetry (DPV) at 10 mV s^{-1}, and rotating disc electrode (RDE) at 100 mV s^{-1} with a rate of 500 rotations per minute (rpm). DPV and RDE measurements were not performed in the solid-state due to desorption of the sample from the electrode.

Compound **1** was immobilized on a glassy carbon electrode as follows. A concentrated suspension of the compound in CH_2Cl_2 was added dropwise onto the electrode surface and allowed to evaporate completely under a N_2 stream. All voltammograms in the solid-state were recorded in MeCN with tetrabutylammonium hexafluorophosphate ($TBAPF_6$, 0.25 M) as the supporting electrolyte. Upon the completion of the measurements, a blank voltammogram was obtained using a clean glassy carbon electrode to confirm no dissolution of any compounds throughout the measurements. Solution-state voltammograms of **3** were obtained at an analyte concentration of 1.0 mM in CH_2Cl_2 with $TBAPF_6$ (0.25 M) as the supporting electrolyte.

Results and discussion

Synthesis

Compounds **1** and **2** were synthesized using similar methods (Scheme 1), with the initial step involving the reaction of equimolar amounts of europium(II) iodide and tpa in MeCN, resulting in a bright orange solution. For **1**, bpym dissolved in MeCN was added to the above solution, immediately resulting in a dark red solution, from which the crystalline product was obtained by layering with either THF or iPr_2O, with a better yield obtained with THF. In contrast, the poor solubility of bptz mandates a different method for **2**, involving a small excess of the bptz ligand suspended in iPr_2O carefully layered on top of the EuI_2 and tpa mixture, which results in very low yields of red crystals of **2**. This reaction involves reduction of bptz to the monoanionic radical form and concomitant oxidation to Eu(III), with compound **2** comprising a monocationic dinuclear complex ($\mathbf{2}^+$) and an iodide counteranion. Complex **3** was synthesized under ambient conditions by reacting $Eu(NO_3)_3$·6H_2O with stoichiometric amounts of tpa and Br_4cat^{2-} in MeCN, which resulted in dark red crystals in good yield. Elemental and thermogravimetric analyses were performed to determine the solvation of bulk samples of compounds **1** and **3** (Fig. S5†). Despite multiple attempts at growing crystals *via*

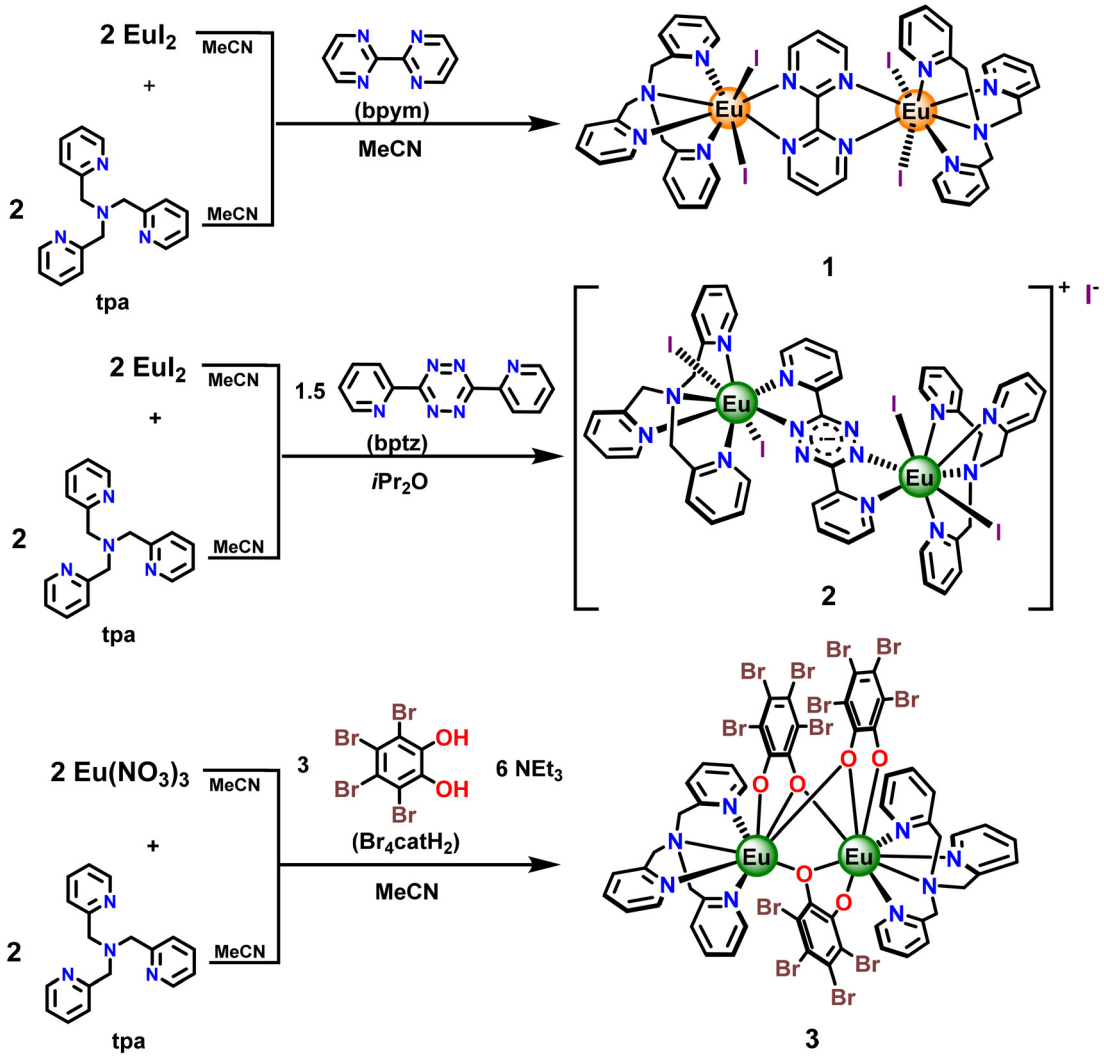

Scheme 1 General synthetic scheme for complexes **1** (top), 2^+ in **2** (middle), and **3** (bottom).

various methods, it was not possible to obtain an analytically pure bulk sample of **2**, so the discussion that follows is limited to a structural investigation only for this compound.

Compound **1** is highly air-sensitive under atmospheric conditions; thus for physical characterization of **1**, the samples were prepared under a N_2 atmosphere. In contrast, **3** is stable under ambient conditions, allowing for straightforward characterization. In all cases, the powder X-ray diffraction patterns of the bulk products are in good agreement with the patterns simulated from single crystal data, consistent with the phase purity of the bulk samples (Fig. S4†). Solution-state characterization of **1** was prevented by poor solubility in all standard solvents. Unlike **1**, **3** is soluble in some common organic solvents and spectroscopic and electrochemical measurements were performed in CH_2Cl_2.

Structure description

The solid-state structures for **1**·2.5MeCN and **3**·MeCN were determined by single-crystal X-ray diffraction at 100 K, while that of **2**·0.7H_2O was determined at 150 K (Fig. 1), with crystallographic details given in Table S1† and average bond lengths and intramolecular and intermolecular distances tabulated in Table 1. All compounds are dinuclear with europium centers bridged with different redox-active ligands – bpym for **1**, $bptz^{\bullet-}$ for **2**, and three Br_4cat^{2-} for **3**. The europium compounds exhibit different metal oxidation states: **1** contains two Eu(II) centers bridged by a closed shell neutral ligand, **2** contains two Eu(III) centers bridged by a monoradical monoanionic ligand, and **3** contains two Eu(III) centers bridged by three diamagnetic dianionic bridging ligands (Fig. S6†).

Compound **1**·2.5MeCN crystallizes in the triclinic $P\bar{1}$ space group. The asymmetric unit contains two different half dinuclear complexes along with MeCN lattice solvent. The structure is thus composed of two distinct centrosymmetric dinuclear complexes (molecule 1 with Eu1 and molecule 2 with Eu2), which are approximately isostructural. Each dinuclear complex is composed of two tpa-coordinated Eu(II) centers bridged by a bipyrimidine ligand, with each Eu(II) also bound to two mono-

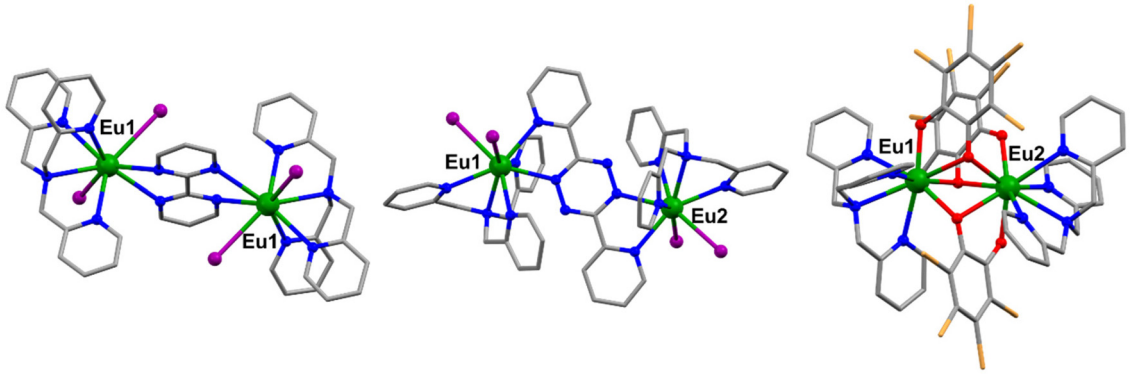

Fig. 1 Molecular structures of one of the two distinct dinuclear complexes in **1** (left), $\mathbf{2}^{+}$ (middle) and **3** (right). Solvent molecules, hydrogen atoms and counter ions are omitted for clarity. Color code: Eu (green), N (blue), O (red), I (purple), Br (orange), and C (grey).

Table 1 Selected interatomic distances (Å) for compounds **1**, **2** and **3**

	1·2.5MeCN		**2**·0.7H_2O		**3**·MeCN	
	Molecule 1 (Eu1)	Molecule 2 (Eu2)	Eu1	Eu2	Eu1[a]	Eu2[b]
Avg. Eu–$N_{bpym/bptz}$	2.766(1)	2.755(8)	2.547(6)	2.548(7)	—	—
Avg. Eu–O_{Cat}	—	—	—		2.374(4)	2.433(4)
Avg. Eu–N_{tpa}	2.726(13)	2.706(13)	2.568(11)	2.561(10)	2.654(4)	2.706(4)
Avg. Eu–I	3.363(1)	3.320(1)	3.115(1)	3.150(1)	—	—
Eu···Eu (intramolecular)	7.118(1)	7.017(1)	7.805(1)		3.633(5)	
Eu···Eu (intermolecular)	10.154(1)		8.968(1)		10.936(3)	

[a] Coordination number of Eu1 center: 8. [b] Coordination number of Eu2 center: 9.

dentate iodo ligands (Fig. S10†). Each Eu(II) center is 8-coordinate with six nitrogen donors (four from the tetradentate tpa ligand and two from the bridging bpym ligand) and two iodo ligands. Continuous shape measurements using the program SHAPE 2.1[54,55] were employed to determine the coordination geometry of the europium centers (Table S3†), indicating a biaugmented trigonal prism (BPTR-8, 2.385) for Eu1 in molecule 1 and a triangular dodecahedron (TDD-8, 2.745) for Eu2 in molecule 2 (Fig. S7†). The average Eu–N_{tpa} and Eu–N_{bpym} bond lengths are 2.716(13) Å and 2.761(8) Å, respectively, consistent with divalent Eu(II) at 100 K.[6] A comparison of the bipyrimidine bridging ligand bond lengths with literature examples is consistent with the ligand being in its neutral state.[56]

Compound **2**·0.7H_2O crystallizes in the orthorhombic *Pbca* space group. The asymmetric unit contains a complete dinuclear complex with two independent Eu(III) centers bridged by the bptz ligand in *trans* coordination mode along with iodide as the counter ion and a partial water molecule. The dinuclear complex is monocationic with each Eu center coordinated to a tpa ligand and two iodo ligands, and with an iodide counterion for charge balance. A partially occupied water molecule of hydration forms hydrogen bonds with the iodide counterion. Shape analysis of **2** suggests a triangular dodecahedron (TDD-8, 2.481/2.616) for both Eu centers (Fig. S8 and Table S3†). The average Eu–N_{tpa} and Eu–N_{bptz} bond lengths are 2.544(8) Å and 2.548(1) Å, respectively, shorter than those of **1**, consistent with Eu(III) at 150 K.[57] The one-electron reduction to $bptz^{\bullet-}$ is consistent with elongation of the N=N bonds within the tetrazine moiety to around 1.383 Å (Fig. 2).[29,58–60]

Compound **3**·MeCN crystallizes in the monoclinic $P2_1/c$ space group. The asymmetric unit consists of a complete dinuclear complex, with two independent Eu(III) centers bridged by three bromocatecholate ligands along with the lattice solvent MeCN. This neutral dinuclear complex has two Eu(III) centers with different coordination numbers, resulting

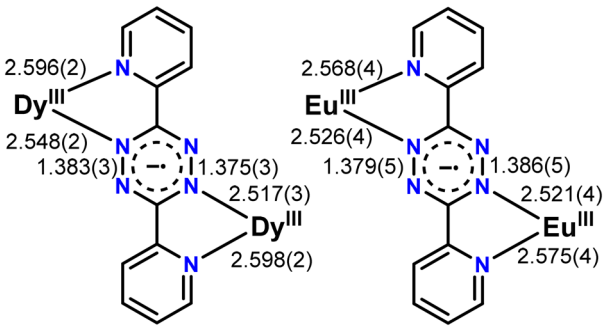

Fig. 2 Structural comparison of the structure fragment in **2** (right) with that of a previously reported Dy $bptz^{\bullet-}$ complex (left) with an equivalent binding mode.[29]

in different coordination geometries. Center Eu1 is 8-coordinate with a biaugmented trigonal prism geometry (BTPR-8, 5.038) and Eu2 is 9-coordinate with a spherical capped square antiprism geometry (CSAPR-9, 2.035) (Fig. S9†). The average Eu–N_{tpa} bond length is 2.654(4) Å/2.706(4) Å and the average Eu–O bond length is 2.406(5) Å, consistent with Eu(III) in both cases.[31] The increase in average Eu–N_{tpa} bond lengths in complex **3** compared to **2** is due to different coordination numbers (8 and 9) for the europium centers. The oxidation state of dioxolene ligands can be determined by empirical metrical oxidation state (MOS) calculations.[61] The MOS values for the bridging ligands in **3** (Table S2†) range between −1.65 and −1.85 (Table S2†), consistent with tetrabromocatecholate rather than the semiquinonate analogue.

For **1**·2.5MeCN, the Eu1 and Eu2 dimers form zig-zag chains *via* I···H–C short links (Fig. S13†) creating a 3D network interlinked *via* short contacts through MeCN solvent molecules. Compound **2**·0.7H_2O exhibits an intricate network of hydrogen bonding interactions between water molecules, iodide counter ions, and cationic dimers, with each iodide ion accepting four short contacts (Fig. S14 and S15†). In contrast, **3**·MeCN displays weaker intermolecular interactions, with neighbouring molecules crosslinked *via* Br···Br interactions forming a chain along direction *c* (Fig. S16†). The intramolecular Eu···Eu distances for dimers of **1** are 7.118(1) and 7.017(1) Å, and 7.805(1) Å for **2**. On the other hand, the Eu···Eu distance for **3** is notably shorter (3.633(5) Å). The nearest neighbour intermolecular Eu···Eu distances are similar for **1** and **3** (10.154(1) and 10.936(3) Å, respectively) and shorter for **2** (7.608(1) Å).

Electronic spectroscopy

As indicated above, the air sensitivity and insolubility of compound **1** in solution restricted electronic spectroscopy to the solid-state, and optical measurements were performed using diffuse reflectance (Fig. 3). Kubelka–Munk transformations involved the Kubelka–Munk equation ($k/s = (1 - R)^2/2R$, where k is the molar absorption coefficient, s is the scattering coefficient, and R is the absolute reflectance of the sample). The maxima and full-width half maxima from the spectra were obtained by deconvoluting the spectra using multi-peak Gaussian fitting (Fig. S18†).

The spectra for all compounds exhibit sharp and intense bands around 235–278 nm, which correspond to the ligand-based charge transfer process (π–π* transitions). Bands in the range 260–278 nm are assigned to tpa ligand-based transition, whereas in the case of **1**·MeCN, they could additionally be due to bpym ligand-based transitions. For **3**, bands at 236 and 306 nm are assigned to Br_4cat^{2-} ligand-based absorption, as can be observed for the free ligand (Fig. S17†). A broad and intense band at 381 nm for **1**·MeCN corresponds to a spin-allowed 4f → 5d transition, which is typical of Eu(II) complexes due to the relative stabilization of 5d orbitals.[6,7] In contrast, for **3**, a broad band at 368 nm likely corresponds to ligand to metal charge transfer (LMCT) transitions from the Br_4cat^{2-} ligand to Eu(III), as seen previously for Eu–tetrabromocatecholate complexes.[62]

The solubility of compound **3** enabled UV-vis measurements, with the spectrum recorded in CH_2Cl_2. The solution spectrum exhibits intense absorption bands in the UV region, corresponding to Br_4cat^{2-} and tpa ligand-based transitions, while an LMCT band appears around 400 nm, similar to that observed in the solid-state spectra (Fig. S19†).

Magnetochemistry

Magnetic susceptibility and magnetization measurements were conducted on **1**·MeCN and **3**·MeCN. Magnetic susceptibility data were acquired between 1.8 and 300 K at 0.1 T (Fig. 4). The measured molar magnetic susceptibility thermal product ($\chi_M T$) for **1**·MeCN between 15 and 300 K of 15.6 cm^3 K

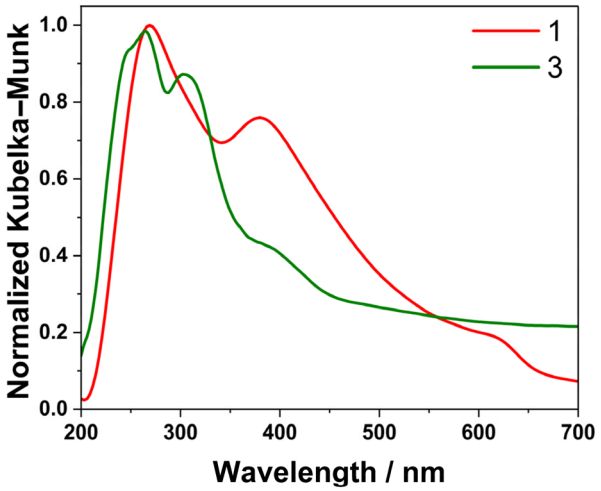

Fig. 3 Diffuse reflectance electronic spectra of compounds **1**·MeCN and **3**·MeCN.

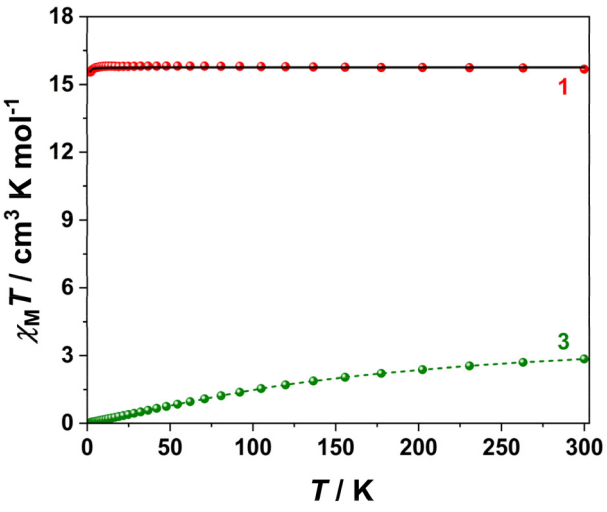

Fig. 4 Magnetic susceptibility data for compounds **1**·MeCN (red) and **3**·MeCN (green) in the range of 1.8–300 K. The black line represents the fit of the data for **1**·MeCN as described in the text. The dashed line for **3**·MeCN are guides for the eye.

mol^{-1} is consistent with the theoretical value of 15.7 cm^3 K mol^{-1} expected for two non-interacting Eu(II) centers ($4f^7$, $^8S_{7/2}$ with g = 2). A small drop in $\chi_M T$ below 10 K can be attributed to the combination of thermal depopulation, spin–orbit contribution, and weak antiferromagnetic inter/intramolecular interactions. The weak nature of these interactions is supported by the intramolecular and intermolecular Eu(II)···Eu(II) distances of 7.118(1) Å and 10.154(1) Å, respectively. To quantify the strength of interactions, the magnetic susceptibility data for **1**·MeCN were fit using PHI,[53] to the spin-only exchange Hamiltonian: $\hat{H} = -2J\cdot\hat{S}_1\cdot\hat{S}_2$, where J represents the intramolecular Eu···Eu exchange coupling and $\hat{S}$ is the spin for each Eu(II) center. The best fit (Fig. S20†) yielded a small exchange coupling constant of J = −0.6 cm^{-1}, which is indicative of weak antiferromagnetic coupling between Eu(II) centers and is consistent with similar systems of isoelectronic Gd(III) complexes with J = −0.04 cm^{-1}.[63,64] The magnetization (Fig. S21†) increases rapidly upon increasing the field, reaching a value of 14.5μ_B at 2 K and 7 T, which is in close agreement with the magnetization value expected for two individual Eu(II) ions.

In marked contrast to **1**·MeCN, $\chi_M T$ values for **3**·MeCN were found to be 2.69 and 0.03 cm^3 K mol^{-1} at 300 and 2 K, respectively. These values are consistent with the presence of Eu(III) ions suggested by the X-ray crystal structure. Although the $^7F_0$ ground term of a Eu(III) ion is non-magnetic, the low lying $^7F_1$ level is generally populated at 80–100 K and non-Curie behaviour is observed. In addition, the low temperature magnetic response of Eu(III) compounds is typically dominated by temperature independent paramagnetism (TIP) due to mixing of the $^7F_1$ and $^7F_2$ multiplets. These factors prohibit straightforward fitting of the magnetic data. The 2 K value of 0.03 cm^3 K mol^{-1} for $\chi_M T$ is consistent with that of two non-magnetic Eu(III) ions.[31] Magnetization measurements at 2 K and 7 T are consistent with the value expected for two individual Eu(III) ions (Fig. S22†).

Electrochemistry

The redox properties of **1** and **3** were investigated using voltammetry. The insolubility of **1** in all standard solvents restricted investigations to solid-state cyclic voltammetry (CV) with powdered samples immobilized on a glassy carbon electrode.[31,65] To the best of our knowledge, this is the first report of solid-state electrochemical studies on a divalent europium complex. On the other hand, the poor stability and solubility of compound **2** prohibited voltammetric investigation. The solubility of compound **3** in CH_2Cl_2 (1.0 mM) allowed for characterisation in solution *via* CV, differential pulse (DPV) and rotating disk electrode (RDE) voltammetry. In all cases, measurements were performed under an N_2 atmosphere and $TBAPF_6$ as a supporting electrolyte in MeCN for **1** and CH_2Cl_2 for **3**. For the cyclic voltammograms, the mid-point potentials (E_m) were determined by taking the average between the peak anodic potential (E_{pa}) and peak cathodic potential (E_{pc}) for the reversible processes, while either the E_{pa} or E_{pc} value was taken for the irreversible processes. For the DPV measurements, the peak potentials (E_p) were taken for all processes. All potentials are quoted *versus* the ferrocenium/ferrocene couple.

The voltammograms recorded for **1**·MeCN attached to the electrode display four redox events: two oxidation processes and two reduction processes (Fig. 5). The oxidation processes are assigned to the sequential one-electron oxidation of Eu(II) to Eu(III), and the reduction processes are assigned to the one electron reduction of bpym to bpym$^{\bullet-}$ followed by a tpa based reduction. The first Eu(II) to Eu(III) oxidation process (I_M) is quasi-reversible and occurs at an E_m of −0.53 V, while the second (II_M) is irreversible with an E_{pa} of −0.00 V (Table 2). These values are within the range of −1.5 to 1.0 V measured previously for Eu(II) complexes in solution.[1,2,6] The oxidation potentials of Eu(II) complexes are highly sensitive to variations in the ligand environment and coordination sphere.[1,6] The bpym reduction to bpym$^{\bullet-}$ (I_{bpym}) is also quasi-reversible and

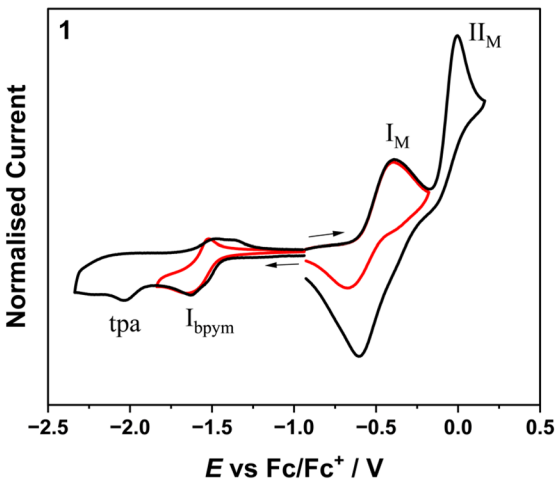

Fig. 5 Solid-state cyclic voltammogram of compound **1**·MeCN attached to a glassy carbon working electrode immersed in MeCN with 0.25 M $TBAPF_6$ at a scan rate of 100 mV s^{-1}. Arrows indicate the starting position and direction of the scan.

Table 2 Voltammetry data for solid **1**·MeCN in MeCN and a solution of **3** in CH_2Cl_2 [a]

Process	CV E_m or E_{pa}/E_{pc}/V	DPV E_p/V
Complex **1**·MeCN		
I_M	−0.533[b]	—
II_M	−0.003[c]	—
I_{bpym}	−1.590[b]	—
tpa	−2.038[d]	—
Complex **3**		
I_M	−1.780[d]	−1.685
II_M	−1.525[d]	−1.415
I_{diox}	—	−0.070
II_{diox}	0.070[c]	0.0450
III_{diox}	0.240[c]	0.135
IV_{diox}	0.380[b]	0.240
V_{diox}	0.565[b]	0.570
tpa	−2.165[d]	—

[a] Potentials reported *vs.* ferrocene/ferrocenium couple. [b] E_m. [c] E_{pa}. [d] E_{pc}.

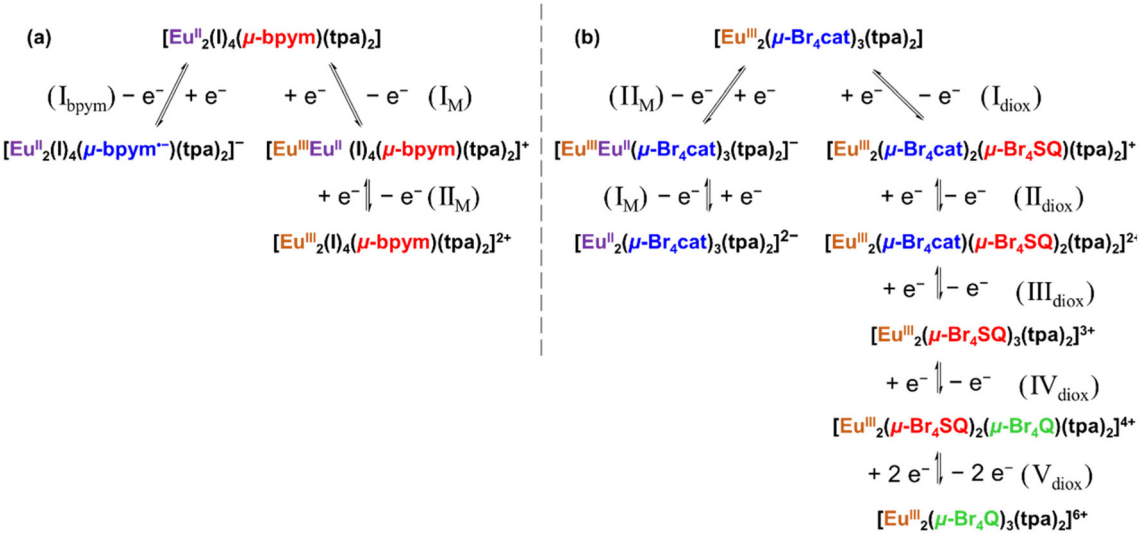

Scheme 2 Assigned redox processes for **1** (left) and **3** (right).

both bpym and tpa ligand reduction potentials are consistent with values reported for literature complexes (Scheme 2).[66]

In comparison, voltammograms for **3** in CH_2Cl_2 solution display eight redox events, with the RDE position of zero current indicating five oxidation and three reduction (Fig. 6 and Fig. S23†) processes. The oxidation processes I_{diox}, II_{diox}, III_{diox}, and IV_{diox} are assigned to sequential one-electron oxidation processes of the three *o*-dioxolene ligands from $\{Br_4cat^{2-}$–Br_4cat^{2-}–$Br_4cat^{2-}\}$ to $\{Br_4cat^{2-}$–Br_4cat^{2-}–$Br_4SQ^{\bullet-}\}$ to $\{Br_4cat^{2-}$–$Br_4SQ^{\bullet-}$–$Br_4SQ^{\bullet-}\}$ to $\{Br_4SQ^{\bullet-}$–$Br_4SQ^{\bullet-}$–$Br_4SQ^{\bullet-}\}$ to $\{Br_4Q^{0}$–$Br_4SQ^{\bullet-}$–$Br_4SQ^{\bullet-}\}$, while V_{diox} is assigned to a two-electron oxidation process of $\{Br_4Q^{0}$–$Br_4SQ^{\bullet-}$–$Br_4SQ^{\bullet-}\}$ to $\{Br_4Q^{0}$–Br_4Q^{0}–$Br_4Q^{0}\}$ as evidenced by DPV (Fig. 6) and RDE (Fig. S23†) measurements. The first two reduction processes, II_M and I_M, are assigned to sequential one-electron reduction of each Eu (III) to Eu(II), with a tpa reduction at a more negative potential. The reduction potentials for the Eu(III) reduction processes are consistent with the values reported in the literature.[30,31]

For both **1** and **3**, the europium-based processes are well separated. For **1**, the separation between the two Eu oxidation is approximately 0.53 V, suggesting significant structural reorganization and changes in the coordination environment of the second Eu(II) center upon the first one-electron oxidation, thereby rendering the subsequent oxidation more challenging. Although analogous dinuclear bpym-bridged Eu(II) complexes have not been reported, Eu(III) analogues are available for comparison. While the dinuclear Eu(III) complex $[\{Eu^{III}(tta)_3\}_2(\mu$-bpym)] (tta = 4,4,4-trifluoro-1-(2-thienyl)-1,3-butanedione)[67] shows a smaller separation of approximately 0.25 V between the first and second Eu(III) reduction processes, $[\{Eu^{III}(tmhd)_3\}_2(\mu$-bpym)][66] (tmhd = 2,2′,6,6′-tetramethyl-2,4-heptanedione) does not exhibit any Eu reduction. This family of related complexes clearly demonstrates the role of the non-bridging ligands in modulating the Eu coordination environment and the sensitivity of the Eu redox potential to this

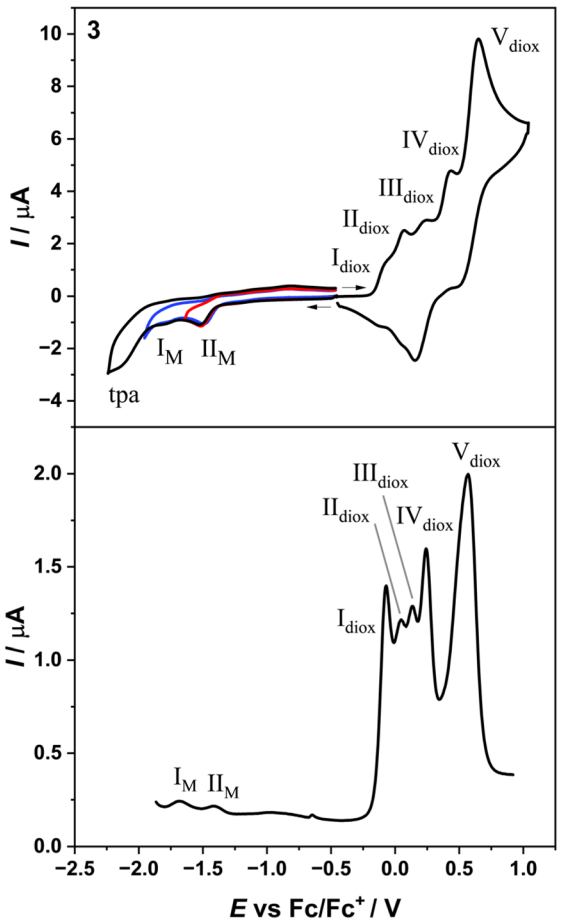

Fig. 6 Voltammograms of compound **3** in CH_2Cl_2 (1.0 mM analyte concentration with 0.25 $TBAPF_6$). Top: cyclic voltammograms obtained with a scan rate of 100 mV s^{-1}. Bottom: differential pulse voltammograms obtained with a scan rate of 10 mV s^{-1}. Arrows indicate the starting position and direction of the scan.

environment. For complex **3**, the europium centers possess distinct coordination environments, which afford the observed differences in their reduction potentials. Eu(II) ions typically adopt a higher coordination number than Eu(III), suggesting that the initial reduction could be favoured at 9-coordinated Eu2.[4] Subsequently, the second reduction occurs at a more negative potential, influenced by both the structural modifications induced by the first reduction and the inherently lower coordination number of Eu1.

With regard to the redox activity of the bridging ligands in the two complexes, **1** displays only the first of two possible bpym reductions within the solvent window. The bpym ligand is known to have two additional oxidation states, $bpym^{\bullet-}$ and $bpym^{2-}$; however, the accessibility of these oxidation states can differ depending on the coordinating metal. Previous electrochemical studies with $[Ln^{III}(tmhd)_3]_2(\mu\text{-bpym})$[66] (Ln = Sm, Eu, and Yb; tmhd = 2,2′,6,6′-tetramethyl-2,4-heptanedione) allows for a comparison with the reductive behaviour of bpym of **1**. The literature complex exhibits two reduction events at *ca.* −1.24 and −1.5 V (E_{pc}) assigned to the sequential one electron reduction of bpym to $bpym^{\bullet-}$ to $bpym^{2-}$. In contrast, **1** exhibits the bpym to $bpym^{\bullet-}$ transition at E_m = −1.60 V. The more negative bpym reduction potential for **1** *versus* the Ln(III) literature compound suggests that coordination to Eu(II) makes reduction of bpym more difficult, which is consistent with previous observations.[68,69] In contrast, all accessible oxidation states for the Br_4cat^{2-} ligands of **3** are readily accessible, with oxidation potentials consistent with literature Br_4cat^{2-} containing complexes.[31]

Conclusions

Herein, we report the synthesis and characterization of three dinuclear Eu complexes $[\{Eu^{II}(I)_2(tpa)\}_2(\mu\text{-bpym})]$ (**1**), $[\{Eu^{III}(I)_2(tpa)\}_2(\mu\text{-bptz}^{\bullet-})][I]$ (**2**), and $[\{Eu^{III}(tpa)_2\}_2(\mu\text{-}Br_4cat)_3]$ (**3**), which exhibit distinct electronic configurations enabled by bridging ligand redox activity. A combination of structural, spectroscopic, magnetic, and electrochemical analyses provides insights into the rich redox chemistry available with these systems. Electrochemical measurements for **1** and **3** reveal multiple redox processes that can be attributed to the bridging ligands and europium ions undergoing both oxidation and reduction. In particular, the redox chemistry of **3** is extremely rich and suggests that a number of different molecular redox states may be accessible. While the three complexes studied here are each internally homovalent, electrochemical studies suggest the possibility of accessing more intricate electronic configurations through mixed-valence analogues, which is the focus of our ongoing investigations. Overall, this study demonstrates the rich and diverse redox chemistry available in molecular polynuclear europium coordination complexes with redox-active ligands, highlighting the versatility and potential of these systems for interesting physical properties and chemical reactivity.

Data availability

All data leading to conclusions presented in this manuscript are included within the manuscript and its ESI.†

Conflicts of interest

There are no conflicts to declare.

Acknowledgements

C. B. thanks the Australian Research Council for funding (DP220100398 and LE210100009). This work was performed in part at the Trace Analysis for Chemical, Earth and Environmental Sciences (TrACEES) Platform at the University of Melbourne. This research was undertaken in part using the MX2 beamline at the Australian Synchrotron, part of ANSTO, Victoria, Australia, and made use of the Australian Cancer Research Foundation (ACRF) detectors. We thank Dr Michael Gardiner, Australian National University (ANU), for the cold mount system at ANSTO. We acknowledge the Australian Research Council for an equipment grant.

References

1 L. A. Basal and M. J. Allen, *Front. Chem.*, 2018, **6**, 1.
2 N. D. H. Gamage, Y. Mei, J. Garcia and M. J. Allen, *Angew. Chem., Int. Ed.*, 2010, **49**, 8923–8925.
3 M. D. Bailey, G. X. Jin, F. Carniato, M. Botta and M. J. Allen, *Chem. – Eur. J.*, 2021, **27**, 3114–3118.
4 E. C. Lewandowski, C. B. Arban, M. P. Deal, A. L. Batchev and M. J. Allen, *Chem. Commun.*, 2024, **60**, 10655–10671.
5 T. C. Jenks, M. D. Bailey, J. L. Hovey, S. Fernando, G. Basnayake, M. E. Cross, W. Li and M. J. Allen, *Chem. Sci.*, 2018, **9**, 1273–1278.
6 M. A. Hay, R. W. Gable and C. Boskovic, *Dalton Trans.*, 2023, **52**, 3315–3324.
7 M. A. Hay and C. Boskovic, *Chem. – Eur. J.*, 2021, **27**, 3608–3637.
8 M. A. Perrin, P. Dutheil, M. Wörle and V. Mougel, *Nat. Commun.*, 2024, **15**, 4577.
9 T. P. Gompa, S. M. Greer, N. T. Rice, N. Jiang, J. Telser, A. Ozarowski, B. W. Stein and H. S. La Pierre, *Inorg. Chem.*, 2021, **60**, 9064–9073.
10 R. M. Diaz-Rodriguez, D. A. Gálico, D. Chartrand, E. A. Suturina and M. Murugesu, *J. Am. Chem. Soc.*, 2022, **144**, 912–921.
11 H. Qi, Z. Zhao, G. Zhan, B. Sun, W. Yan, C. Wang, L. Wang, Z. Liu, Z. Bian and C. Huang, *Inorg. Chem. Front.*, 2020, **7**, 4593–4599.
12 M. I. Ustinova, L. A. Frolova, A. V. Rasmetyeva, N. A. Emelianov, M. N. Sarychev, G. V. Shilov, P. P. Kushch, N. N. Dremova, G. A. Kichigina, A. I. Kukharenko,

D. P. Kiryukhin, E. Z. Kurmaev, I. S. Zhidkov and P. A. Troshin, *J. Mater. Chem. A*, 2024, **12**, 13219–13230.
13 Y. Kim, H. Ohmagari, A. Saso, N. Tamaoki and M. Hasegawa, *ACS Appl. Mater. Interfaces*, 2020, **12**, 46390–46396.
14 I. L. Fedushkin, O. V. Maslova, A. G. Morozov, S. Dechert, S. Demeshko and F. Meyer, *Angew. Chem., Int. Ed.*, 2012, **51**, 10584–10587.
15 N. Jori, D. Toniolo, B. C. Huynh, R. Scopelliti and M. Mazzanti, *Inorg. Chem. Front.*, 2020, **7**, 3598–3608.
16 J. K. Molloy, C. Philouze, L. Fedele, D. Imbert, O. Jarjayes and F. Thomas, *Dalton Trans.*, 2018, **47**, 10742–10751.
17 G. P. Bedwell, N. Suryadevara, Z. Qi, R. W. Gable, P. Bencok, M. L. Baker and C. Boskovic, *Inorg. Chem.*, 2025, **64**, 6519–6530.
18 W. R. Reed, M. A. Dunstan, R. W. Gable, W. Phonsri, K. S. Murray, R. A. Mole and C. Boskovic, *Dalton Trans.*, 2019, **48**, 15635–15645.
19 C. A. Gould, E. Mu, V. Vieru, L. E. Darago, K. Chakarawet, M. I. Gonzalez, S. Demir and J. R. Long, *J. Am. Chem. Soc.*, 2020, **142**, 21197–21209.
20 S. Demir, I. R. Jeon, J. R. Long and T. D. Harris, *Coord. Chem. Rev.*, 2015, **289–290**, 149–176.
21 S. Demir, M. I. Gonzalez, L. E. Darago, W. J. Evans and J. R. Long, *Nat. Commun.*, 2017, **8**, 2144.
22 S. Demir, J. M. Zadrozny, M. Nippe and J. R. Long, *J. Am. Chem. Soc.*, 2012, **134**, 18546–18549.
23 M. A. Dunstan, E. Rousset, M.-E. Boulon, R. W. Gable, L. Sorace and C. Boskovic, *Dalton Trans.*, 2017, **46**, 13756–13767.
24 F. Benner and S. Demir, *Inorg. Chem. Front.*, 2023, **10**, 4981–4992.
25 F. Benner, L. La Droitte, O. Cador, B. Le Guennic and S. Demir, *Chem. Sci.*, 2023, **14**, 5577–5592.
26 P. Zhang, R. Nabi, J. K. Staab, N. F. Chilton and S. Demir, *J. Am. Chem. Soc.*, 2023, **145**, 9152–9163.
27 J. D. Rinehart, M. Fang, W. J. Evans and J. R. Long, *J. Am. Chem. Soc.*, 2011, **133**, 14236–14239.
28 P. Zhang, M. Perfetti, M. Kern, P. P. Hallmen, L. Ungur, S. Lenz, M. R. Ringenberg, W. Frey, H. Stoll, G. Rauhut and J. van Slageren, *Chem. Sci.*, 2018, **9**, 1221–1230.
29 B. S. Dolinar, S. Gómez-Coca, D. I. Alexandropoulos and K. R. Dunbar, *Chem. Commun.*, 2017, **53**, 2283–2286.
30 M. A. Dunstan, N. Suryadevara, L. Cameron, R. W. Gable, M. Massi and C. Boskovic, *Eur. J. Inorg. Chem.*, 2024, e202400113.
31 E. Rousset, M. Piccardo, R. W. Gable, M. Massi, L. Sorace, A. Soncini and C. Boskovic, *Inorg. Chem.*, 2022, **61**, 14004–14018.
32 I. L. Fedushkin, D. S. Yambulatov, A. A. Skatova, E. V. Baranov, S. Demeshko, A. S. Bogomyakov, V. I. Ovcharenko and E. M. Zueva, *Inorg. Chem.*, 2017, **56**, 9825–9833.
33 M. Zou and K. M. Waldie, *Inorg. Chem. Front.*, 2024, **11**, 5795–5809.
34 A. G. Blackman, *Eur. J. Inorg. Chem.*, 2008, 2633–2647.
35 Y. Zang, J. Kim, Y. Dong, E. C. Wilkinson, E. H. Appelman and L. Que, *J. Am. Chem. Soc.*, 1997, **119**, 4197–4205.
36 A. Beni, A. Dei, S. Laschi, M. Rizzitano and L. Sorace, *Chem. – Eur. J.*, 2008, **14**, 1804–1813.
37 K. G. Alley, G. Poneti, P. S. D. Robinson, A. Nafady, B. Moubaraki, J. B. Aitken, S. C. Drew, C. Ritchie, B. F. Abrahams, R. K. Hocking, K. S. Murray, A. M. Bond, H. H. Harris, L. Sorace and C. Boskovic, *J. Am. Chem. Soc.*, 2013, **135**, 8304–8323.
38 J. T. Janetzki, M. G. Chegerev, G. K. Gransbury, R. W. Gable, J. K. Clegg, R. J. Mulder, G. N. L. Jameson, A. A. Starikova and C. Boskovic, *Inorg. Chem.*, 2023, **62**, 15719–15735.
39 J. Andrez, G. Bozoklu, G. Nocton, J. Pécaut, R. Scopelliti, L. Dubois and M. Mazzanti, *Chem. – Eur. J.*, 2015, **21**, 15188–15200.
40 H. T. Balaydin, Y. Akbaba, A. Menzek, E. Şahin and S. Göksu, *ARKIVOC*, 2010, **2009**, 75–87.
41 H. Bakkali, C. Marie, A. Ly, C. Thobie-Gautier, J. Graton, M. Pipelier, S. Sengmany, E. Léonel, J. Y. Nédélec, M. Evain and D. Dubreuil, *Eur. J. Org. Chem.*, 2008, 2156–2166.
42 P. F. H. Schwab, F. Fleischer and J. Michl, *J. Org. Chem.*, 2002, **67**, 443–449.
43 Rigaku Oxford Diffraction, *CryaAlisPro Software, version 1.171.42.72a*, Rigaku Corporation, Wroclaw (Poland), 2022.
44 D. Aragão, J. Aishima, H. Cherukuvada, R. Clarken, M. Clift, N. P. Cowieson, D. J. Ericsson, C. L. Gee, S. Macedo, N. Mudie, S. Panjikar, J. R. Price, A. Riboldi-Tunnicliffe, R. Rostan, R. Williamson and T. T. Caradoc-Davies, *J. Synchrotron Radiat.*, 2018, **25**, 885–891.
45 W. Kabsch, *Struct. Biol.*, 2010, **66**, 125–132.
46 F. van den Akker and W. G. J. Hol, *Acta Crystallogr., Sect. D: Biol. Crystallogr.*, 1999, **55**, 206–218.
47 A. J. Thompson, K. M. L. Smith, J. K. Clegg and J. R. Price, *J. Appl. Crystallogr.*, 2023, **56**, 558–564.
48 G. M. Sheldrick, *Acta Crystallogr., Sect. A:Found. Adv.*, 2015, **71**, 3–8.
49 G. M. Sheldrick, *Struct. Chem.*, 2015, **71**, 3–8.
50 G. M. Sheldrick, *Acta Crystallogr., Sect. C:Struct. Chem.*, 2015, **71**, 3–8.
51 O. V. Dolomanov, L. J. Bourhis, R. J. Gildea, J. A. K. Howard and H. Puschmann, *J. Appl. Crystallogr.*, 2009, **42**, 339–341.
52 G. A. Bain and J. F. Berry, *J. Chem. Educ.*, 2008, **85**, 532–536.
53 N. F. Chilton, R. P. Anderson, L. D. Turner, A. Soncini and K. S. Murray, *J. Comput. Chem.*, 2013, **34**, 1164–1175.
54 D. Casanova, J. Cirera, M. Llunell, P. Alemany, D. Avnir and S. Alvarez, *J. Am. Chem. Soc.*, 2004, **126**, 1755–1763.
55 M. Pinsky and D. Avnir, *Inorg. Chem.*, 1998, **37**, 5575–5582.
56 G. Zucchi, P. Thuéry, E. Rivière and M. Ephritikhine, *Chem. Commun.*, 2010, **46**, 9143–9145.
57 R. Wietzke, M. Mazzanti, J. M. Latour, J. Pécaut, P. Y. Cordier and C. Madic, *Inorg. Chem.*, 1998, **37**, 6690–6697.
58 M. A. Lemes, N. Mavragani, P. Richardson, Y. Zhang, B. Gabidullin, J. L. Brusso, J. O. Moilanen and M. Murugesu, *Inorg. Chem. Front.*, 2020, **7**, 2592–2601.

59 B. S. Dolinar, D. I. Alexandropoulos, K. R. Vignesh, T. James and K. R. Dunbar, *J. Am. Chem. Soc.*, 2018, **140**, 908–911.
60 N. Mavragani, A. A. Kitos, J. Hrubý, S. Hill, A. Mansikkamäki, J. O. Moilanen and M. Murugesu, *Inorg. Chem. Front.*, 2023, **10**, 4197–4208.
61 S. N. Brown, *Inorg. Chem.*, 2012, **51**, 1251–1260.
62 A. M. Atkin, M. J. Giansiracusa, S. Calvello, E. Rousset, R. W. Gable, W. Phonsri, K. S. Murray, J. K. Howard, A. Soncini, R. A. Mole and C. Boskovic, *Inorg. Chem.*, 2023, **62**, 1141–1155.
63 D. Errulat, R. Marin, D. A. Gálico, K. L. M. Harriman, A. Pialat, B. Gabidullin, F. Iikawa, O. D. D. Couto, J. O. Moilanen, E. Hemmer, F. A. Sigoli and M. Murugesu, *ACS Cent. Sci.*, 2019, **5**, 1187–1198.
64 D. Visinescu, L. M. Toma, O. Fabelo, C. Ruiz-Pérez, F. Lloret and M. Julve, *Inorg. Chem.*, 2013, **52**, 1525–1537.
65 S. Bagio, J. González, R. W. Gable, C. R. Hall, C. Boskovic and M. J. Giansiracusa, *Dalton Trans.*, 2025, **54**, 5061–5074.
66 M. H. Baker, J. D. Dorweiler, A. N. Ley, R. D. Pike and S. M. Berry, *Polyhedron*, 2009, **28**, 188–194.
67 R. Sultan, K. Gadamsetti and S. Swavey, *Inorg. Chim. Acta*, 2006, **359**, 1233–1238.
68 M. H. Baker, J. D. Dorweiler, A. N. Ley, R. D. Pike and S. M. Berry, *Polyhedron*, 2009, **28**, 188–194.
69 D. K. Modder, M. S. Batov, T. Rajeshkumar, A. Sienkiewicz, I. Zivkovic, R. Scopelliti, L. Maron and M. Mazzanti, *Chem. Sci.*, 2022, **13**, 11294–11303.